scientific reports

Check for updates

OPEN

# Simulation and experimental study on processing behavior of coronary artery calcified tissue removal

Chuhang Gao[1,2], Jialiang Zhu[1,2], Fan Wu[1,2], Ziyu Cui[1,2], Mingcheng Fang[3,4,5]✉, Zhaoju Zhu[1,2]✉ & Bingwei He[1,2]

**Coronary artery atherosclerosis is a prevalent cardiovascular disease and a leading cause of major adverse cardiovascular events (MACE). Rotational atherectomy (RA) is an effective interventional technique for treating severe calcified stenosis. However, excessive forces, heat, and debris are prone to lead to serious surgical complications, such as slow flow/no-reflow and blood clots. To mitigate excessive force and heat generation during RA, a novel high-performance cutting tool was designed and fabricated for coronary artery calcified tissue removal. An RA simulation model was developed to simulate the procedure. The results showed that the forces, temperatures, and debris size remained within predefined safety thresholds. Using the 1.5 mm tool as an illustration, the peak cutting force was 1.062 N, and the peak temperature rise reached 1.170 °C. Debris distribution exhibited a normal pattern, with 90% of particles measuring below 14 µm. The experimental results closely matched the simulation values, showcasing errors under 10% and affirming the simulation model's precision. This research provides theoretical support for the study of mechanisms and contributes to optimizing the effectiveness of RA.**

**Keywords** Rotational atherectomy, Tissue removal, Cutting performance, Finite element simulation

Atherosclerosis is a chronic disease characterized by the progressive accumulation of cholesterol and lipid substances, resulting in the formation of atherosclerotic plaques[1]. Over time, these plaques undergo volumetric expansion and calcification. This process is accompanied by chronic inflammation and cellular apoptosis. Ultimately, it results in the narrowing or complete occlusion of the blood vessels, leading to major adverse cardiovascular events (MACE)[2,3]. Percutaneous coronary intervention (PCI) is the primary treatment approach for vascular blockages. It is commonly used for the early-stage plaques with a softer tissue texture. The procedure involves balloon angioplasty along with stent implantation to restore blood flow[4]. However, in cases of vascular calcification, symptoms may be challenging to detect until the disease has progressed to a severe calcified stage, requiring RA as the preferred treatment[5,6].

RA is a catheter-based procedure that utilizes a high-speed cutting tool (usually operating at 80,000 to 170,000 rpm) to cut and remove calcified tissue, aiming to restore blood flow by expanding the vessel lumen[7]. Previous studies have shown that the primary patency rate of RA can reach 99% in the first 12 months after surgery and 83% at 24 months[8]. In particular, for chronic total occlusion lesions with severe calcification, RA demonstrates a high procedural success rate and yields excellent long-term clinical outcomes[9,10]. When compared to standalone PCI, incorporating RA for lesion preparation facilitates optimal stent and balloon expansion, thereby enhancing the treatment success rate[11,12].

Although RA is an effective treatment, there is still a risk of bodily harm of tools and drive shafts entering the body as foreign objects[13,14]. Common surgical complications include vascular rupture, dissection, no reflow/slow flow, and thrombus[15–17]. Improper RA parameters have been identified as a major factor in surgical complications. Excessive forces can lead to vascular endothelium rupture, allowing blood entry into the arterial wall through the rupture site, forming a hematoma, and potentially resulting in vascular dissection[18]. Excessive debris may obstruct the distal capillaries, resulting in impaired blood circulation and secondary occlusion[19]. Elevated temperature in the cutting area can induce blood aggregation, leading to thrombus formation, which poses a life-threatening risk to patients[20].

[1]School of Mechanical Engineering and Automation, Fuzhou University, Fuzhou 350108, China. [2]Fujian Engineering Research Center of Joint Intelligent Medical Engineering, Fuzhou 350108, China. [3]Fujian Provincial Hospital, Fuzhou 350001, China. [4]Department of Cardiology, Fujian Provincial Hospital, Fuzhou 350001, China. [5]Fuzhou University Town, No. 2 Wulongjiang North Avenue, Fuzhou City, Fuzhou, Fujian Province, China. ✉email: 461686552@qq.com; zhuzhaoju0216@163.com

To enhance the efficiency of RA, several researchers are researching on the mechanisms and developing novel surgical instruments. Shammas et al.[21] performed RA on 40 patients with severe vascular calcification. They incorporated fragment filters at the front of the cutting area and found that 18 filters captured fragments with a diameter ≥ 2 mm. Gehani et al.[22] utilized an infrared imaging system to detect heat during RA of the porcine aorta. They found that the average temperature rise was 52.8 ± 16.9 °C without blood cooling and 11.8 ± 2.9 °C with blood cooling at 18 ml/min. These results suggest that RA generates a significant amount of heat, which can be effectively mitigated by the circulation of blood. NAKAO et al.[23] proposed a novel RA tool with a 5-micron bump on its surface and tested it on eggs at 150,000 rpm. The tool effectively removed the eggshell without damaging the egg white, aligning with the principle of "differential cutting." ZHENG et al.[24] calculate the impact force between the tool and the calcified tissue based on the Hertz contact model. They established a multi-grain smoothed particle hydrodynamics model to simulate the cutting force. At 135,000, 155,000, and 175,000 rpm, the simulation predicted cutting forces of 41, 51, and 99 mN, respectively, with relative errors below 10% compared to experimental data. KIM et al.[25] employed laser engraving technology to texture cutting tools, achieving rough surfaces. Cutting tests on Hydroxyapatite/Polylactic Acid (HA/PLA) composite and rubber at 120,000 rpm showed a maximum force of 0.72 ± 0.12 N for HA/PLA, with no damage to the rubber material. ZHU et al.[26] utilized computational fluid dynamics to investigate the vessel shear stress during RA. They found that with a tool diameter to vessel diameter ratio (B/A) below 0.5, the flow field remains stable. For a 4.5 mm tool at 170,000 rpm, the pressure and shear stress were 92.77 kPa and 10.36 kPa, respectively.

The above researches provide valuable references for this paper. However, the relationship between RA process parameters and results remains unclear. This study focuses on the mechanism and processing characteristics of RA. By integrating simulation and experimental analysis, the research thoroughly explores the influence of RA process parameters on the results. First, an RA experimental platform was constructed, and a novel cutting tool was proposed. Secondly, a simulation RA model was established and the model's validity was confirmed by comparing it with experimental data. Finally, according to the experimental and simulation results, the tool motion law was summarized and the force analysis was carried out. The effect of RA parameters on force, temperature, and debris morphology was systematically expounded. The feasibility of the tool and the accuracy of the simulation model were verified. This research provides guidance for optimizing the effectiveness of RA.

## Materials and methods

### Experimental setup

The experimental platform is shown in Fig. 1, consisting of power equipment, fluid delivery pipeline, force measurement device, temperature measurement system, and tool motion trajectory measurement system.

The power equipment is a high-performance surgical device powered by a coreless motor, which can drive a flexible drive shaft at high speed. The liquid delivery system includes a thermostatic water tank set at 37℃ (equivalent to core body temperature), a soft Polyvinyl chloride (PVC) tube, and a peristaltic pump. Fresh bovine bone demonstrates mechanical properties that closely approximate those of calcified human tissue. Therefore, it was selected as a simulated model for calcified tissue. The bone processing procedure is illustrated in Fig. 2(a). Following cutting and core extraction, the bone is shaped into a regular cylinder. Subsequently, a high-speed drill and a straight reamer are used to create an inner bore with a diameter of 4 mm. The Acrylic

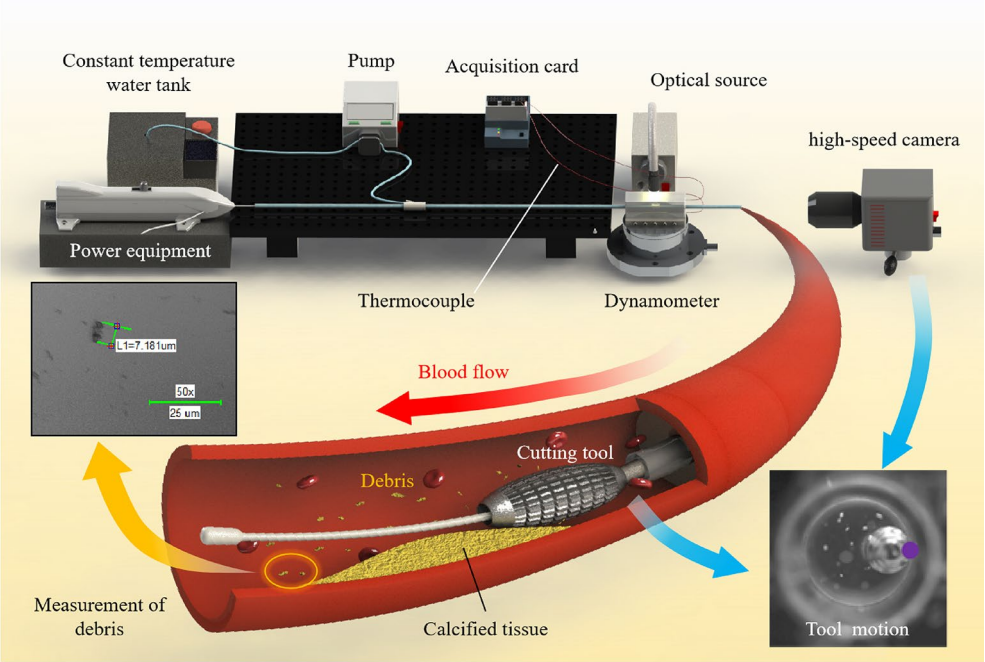


**Fig. 1**. Experimental setup.

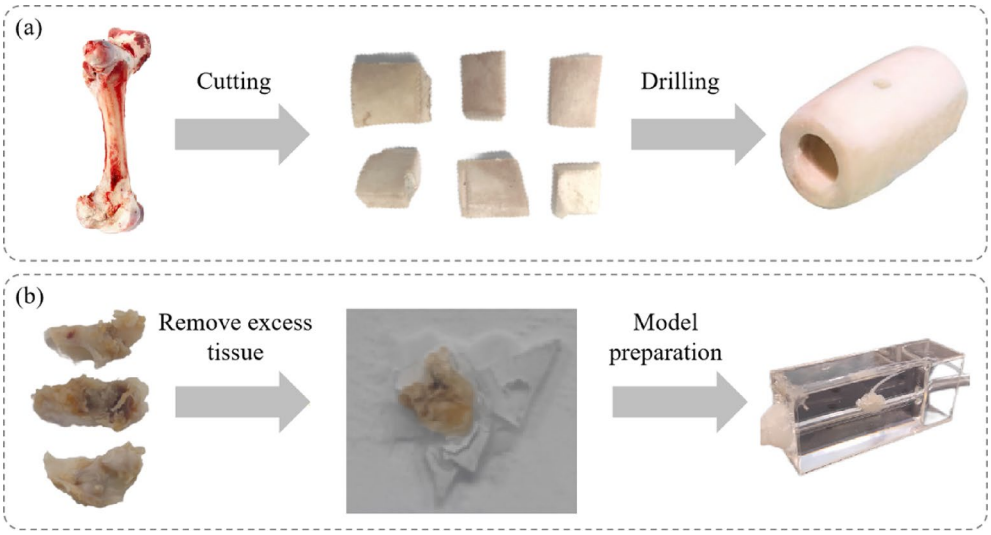


**Fig. 2**. Experimental materials preparation. (**a**) Bone processing, (**b**) Calcified tissue preprocessing and packaging.

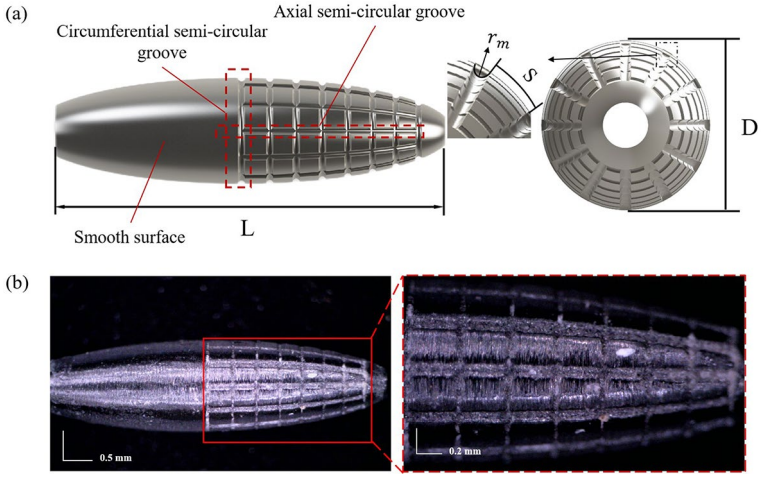


**Fig. 3**. Digital models and prepared tool. (**a**) Tool model and size description, and (**b**) prepared tool.

shell and epoxy resin filler were used to encapsulate the bone to make the measurement model. The cutting force was measured using a high-precision piezoelectric force sensor (Model 9272, Kistler, Switzerland) positioned beneath the measurement model. The force data were filtered using Dynoware software (Version 3.1.2.0, Kistler, Switzerland). Temperature was collected using two K-type thermocouples (5 TC-TT-K-40-36, Omega, USA), positioned 180° apart circumferentially within the model, and the data were captured using a data acquisition card (NI-9219, National Instruments, USA). This study obtained human calcified tissue from Fujian Medical University Union Hospital. The processing procedure for calcified tissue is illustrated in Fig. 2(b). The samples were soaked and cleaned in saline solution. Fixatives were used to maintain the morphology and structure. Finally, a dehydration process was carried out by progressively increasing the concentration of alcohol, followed by embedding the samples in a resin embedding agent.

## Accordance statement

This study was performed in line with the principles of the Declaration of Helsinki. We confirm that all methods and experiments were carried out in accordance with relevant guidelines and regulations, and informed consent was obtained from all subjects. Ethical approval was obtained from the Fujian Medical University Union Hospital (Approval number: 2024 KY187).

316 L stainless steel was selected as the tool material. Fabricated via precise metal 3D printing, the tool's structure is depicted in Fig. 3(a) and the prepared tool is shown in Fig. 3(b). Featuring an elliptical shape, the tool minimizes friction and fluid resistance with the surrounding medium. The tool's front section is covered with semicircular grooves in circumferential and axial directions. The sharp micro-edges of the semicircular

| Type | D (mm) | L (mm) | m (g) | S (mm) | $r_m$ (mm) |
|---|---|---|---|---|---|
| 1 | 1.25 | 4.41 | 0.019 | 0.29 | 0.05 |
| 2 | 1.5 | 5.52 | 0.036 | 0.34 | 0.05 |
| 3 | 1.75 | 6.60 | 0.062 | 0.39 | 0.05 |
| 4 | 2.0 | 7.65 | 0.103 | 0.44 | 0.05 |

**Table 1**. Tool structural parameters.

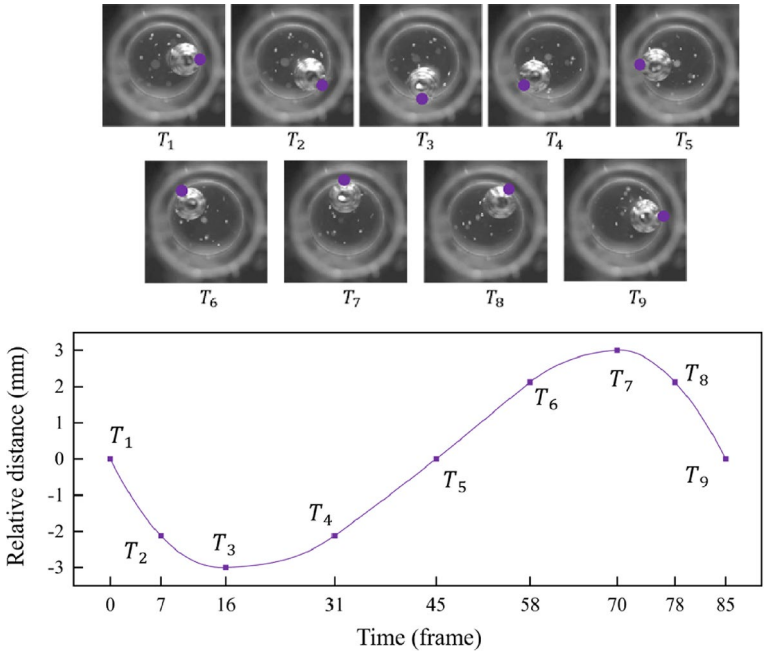


**Fig. 4**. Tool orbit motion trajectory.

grooves can play the role of cutting edge, which can help to improve the material removal rate. To study the influence of tool size changes on cutting results, this paper prepared four commonly used sizes of the tool, the tool parameters are shown in Table 1.

## Tool kinematics analysis

*Tool motion trajectory analysis*

The tool's movement pattern is essential for studying the RA mechanism. The motion trajectory was captured using a high-speed camera. Figure 4 shows the tool motion trajectory for one cycle and the relative displacement at different time points.

From Fig. 4, it can be observed that the tool rotates around its axis while simultaneously orbiting along the vascular wall. This motion arises when the tool's rotational axis bends under unbalanced torque, creating a swirling movement pattern. A complete orbit motion cycle was divided into 9 phases, and the purple markers indicate the contact and collision positions. The tool movement pattern can be described as "collision-rebound-recollision." Fig. 4 also reveals that the tool's moving speed increases and the movement interval shortens as the relative position decreases. This phenomenon is attributed to the influence of gravity on the tool, which will be excluded as an interfering factor in subsequent experiments. Through repeated experiments, it has been observed that the tool's movement period remains constant at a consistent speed. Therefore, the orbit motion frequency at different speeds can be calculated, as shown in Table 2.

*Tool kinematics model*

Based on the tool's kinematic analysis, this study combines the steady-state vortex model for a single-disc rotor[27] to analyze the mathematical relationship between the tool's rotational frequency and orbit frequency. First, the tool's motion coordinate system is established, as shown in Fig. 5.

The coordinates of the rotor's axis $O'$, denoted by ($x$、 $y$), along with the rotational angles $\theta_x$、 $\theta_y$, represent the instantaneous position of the rotor during its motion. Specifically, the rotational angle $\theta_y$ is equivalent to the Euler angle α, while the rotational angle $\theta_x$ is in the opposite direction, and therefore can be expressed as -$\beta$. The rotational angular velocity is denoted by $\Omega$, the polar moment of inertia by $J_p$, the angular momentum by $H = J_p\Omega$, the diametric moment of inertia by $J_d$, and the mass by $m$. The differential equation describing the vortex motion of the cantilever rotor in fixed coordinates can be expressed as shown in Eq. (1).

| Tool diameter | Rotational speed/rpm | Orbit motion frequency/Hz | Tool diameter | Rotational speed/rpm | Orbit motion frequency/Hz |
|---|---|---|---|---|---|
| 1.25 | 60,000 | 414.62 | 1.75 | 60,000 | 227.06 |
| | 80,000 | 420.95 | | 80,000 | 249.00 |
| | 100,000 | 459.94 | | 100,000 | 270.95 |
| | 120,000 | 575.26 | | 120,000 | 316.29 |
| 1.5 | 60,000 | 254.71 | 2.0 | 60,000 | 127.06 |
| | 80,000 | 286.55 | | 80,000 | 129.00 |
| | 100,000 | 333.93 | | 100,000 | 140.95 |
| | 120,000 | 373.62 | | 120,000 | 176.29 |

**Table 2**. Orbit motion frequency of each tool under different speed.

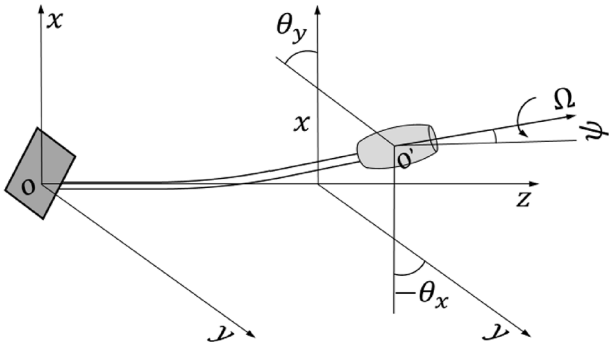


**Fig. 5**. Tool coordinate system.

$$\begin{cases} m\ddot{x} + k_{11}x + k_{14}\theta_y = 0 \\ m\ddot{y} + k_{22}y + k_{23}\theta_x = 0 \\ J_d\ddot{\theta}_x + H\dot{\theta}_y - k_{32}y + k_{33}\theta_x = 0 \\ J_d\ddot{\theta}_y + H\dot{\theta}_x - k_{41}x + k_{44}\theta_y = 0 \end{cases} \tag{1}$$

Where $k$ is the external force or torque applied when a unit angle is generated in different directions. When $\theta_x = -\beta$, $\theta_y = \alpha$, and the rotational axis is a circular cross-section axis, the following relationships hold for the stiffness coefficients:

$$k_{11} = k_{22} = k_{rr}, k_{33} = k_{44} = k_{\phi\phi}, k_{14} = k_{41} = k_{23} = k_{32} = k_{r\phi} = k_{\phi r}$$

Let the tool have eccentricity $e$,initial phase number $\phi_0$. Introducing a complex variable $z = x + iy$ and $\psi = \theta_y - i\theta_x$, the equation becomes

$$m\ddot{z} + k_{rr}z + k_{r\phi}\psi = em\Omega^2 e^{i(\Omega t+\phi_0)} J_d\ddot{\psi} - iH\dot{\psi} + k_{r\phi}z + k_{\phi\phi}\psi = 0 \tag{2}$$

Since the cross-section of the rotating shaft is a circular cross-section, making the right end of the above Eq. 0 gives:

$$m\ddot{z} + k_{rr}z + k_{r\phi}\psi = 0 J_d\ddot{\psi} - iH\dot{\psi} + k_{r\phi}z + k_{\phi\phi}\psi = 0 \tag{3}$$

Let the equation be solved for $z = z_0 e^{iw_n t}$, $\psi = \psi_0 e^{iw_n t}$, which is obtained by substituting into the above equation:

$$\left(-w_n^2 + w_{rr}^2\right) z_0 + w_{r\phi}^2 \psi_0 = 0 w_{\phi r}^2 z_0 + (-w_n^2 + J_p/J_d \Omega w_n + w_{\phi\phi}^2)\psi_0 = 0 \tag{4}$$

The characteristic equation (frequency equation) of the above equation is:

$$\left(-w_n^2 + w_{rr}^2\right)\left(-w_n^2 + J_p/J_d \Omega w_n + w_{\phi\phi}^2\right) - w_{r\phi}^2 w_{\phi r}^2 = 0 \tag{5}$$

This is the equation of the precession of the angular velocity $w_n$, given the value of $\Omega$, we can find the four values of $w_n$. Each solution corresponds to a different mode diagram, as shown in Fig. 6.

Since the tool rotation system can be stabilized only below the first-order critical speed, the first-order vibration mode of the tool thus becomes the stabilizing solution to the equations of the system. This motion

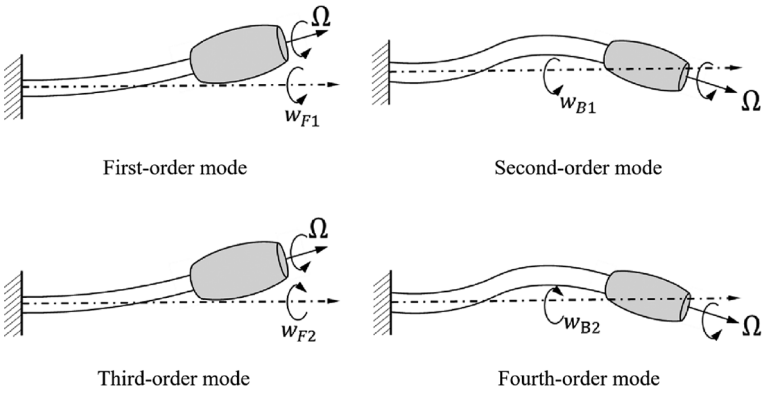


**Fig. 6**. Mode of tool vibration.

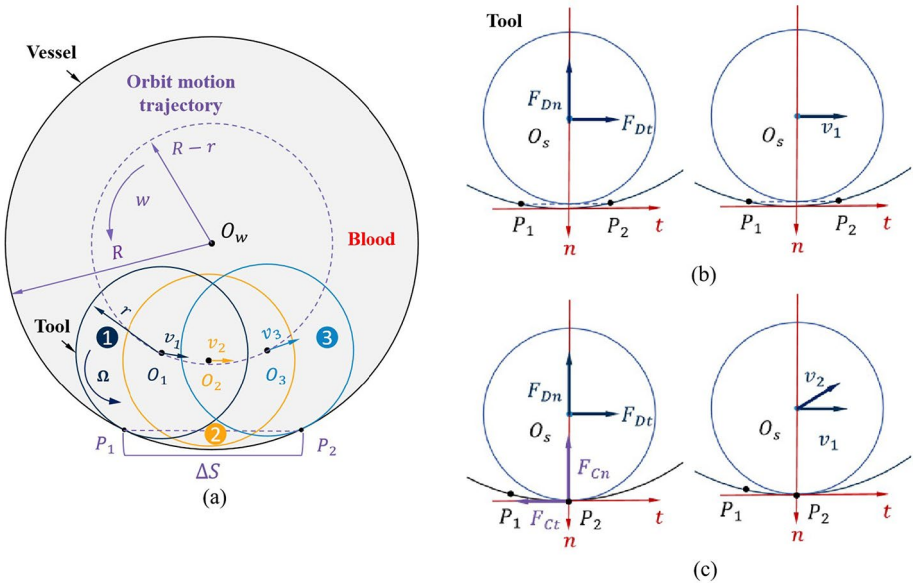


**Fig. 7**. The cutting tool force analysis. (**a**) Schematic diagram of tool motion, (**b**) force and velocities during tool bouncing, and (**c**) force and velocities at tool collision.

mode involves the tool rotating around its equilibrium axis in the same direction as the tool itself, ensuring the system's stability.

## Tool dynamics model

*The tool force analysis*

Based on the tool motion pattern, the tool's motion behavior can be simplified, as shown in Fig. 7(a). In the intermittent cutting process, the tool initially completes ablation at point $P_1$ before transitioning to $P_2$. The tool remains suspended in the blood, as indicated by the yellow position in Fig. 7(a), without contacting the vessel wall or calcified tissue. The force analysis during this stage is illustrated in Fig. 7(b). The tool is primarily influenced by the fluid dynamic pressure $F_D$, with tangential and normal components labeled as $F_{D,t}$ and $F_{D,n}$, respectively.

The tool accelerates in the liquid, and then moves towards $P_1$ in a straight line at a constant velocity $v$. When the tool reaches $P_2$, it is located at the blue position shown in Fig. 7(a). The force and velocity diagrams are illustrated in Fig. 7(c). When the tool is affected by the collision force, the cutting force is generated due to the friction on the surface of the calcified tissue caused by the rotation motion, including its tangential component of $F_{C,t}$ and the normal component of $F_{C,n}$. The resultant force of the screwing tool in collision is shown in Eq. (6) :

$$F = \sqrt{(F_M + F_{C,n} + F_{D,n})^2 + (F_{C,t} + F_{D,t})^2} \tag{6}$$

After leaving point $P_2$, the tool's velocity becomes $v_2$, calculated by Eq. (7). The angle $\alpha$, which represents the change in velocity direction, is determined by the average distance $\Delta S$ between adjacent scratches on the surface of the calcified tissue. This distance is related to the velocity change and can be calculated using Eq. (8).

$$v_1 \approx w(R-r) \tag{7}$$

$$\alpha = \frac{\beta}{2} \approx 2\Delta S/R - r \tag{8}$$

*Differential cutting*

During rotation, the tool induces surrounding blood flow, forming a hydrodynamic pressure film between the tool and the vascular wall. Ideally, the film thickness should be less than the height of the surface particles for effective material removal. When the tool interacts with normal blood vessels, it is necessary to ensure the film thickness is greater than the micro-edge height of the tool surface to avoid damage to healthy blood vessels. Hamrock et al.[28] provide the method to calculate the hydrodynamic pressure model, as shown in the formula (9) :

$$H = 7.43R_E U^{0.65} W^{-0.21}(1 - 0.85e^{-0.31} \tag{9}$$

The relevant physical quantities are as follows:

$$\begin{cases} R_0 = (1/r + 1/R)^{-1} \\ U = v\mu_0/ER_0 \\ W = w/ER_0{}^2 \\ v = \sqrt{v_1^2 + v_2^2} \\ E_0 = 2\left((1-\mu_1^2)/E_1 + (1-\mu_2^2)/E_2\right)^{-1} \end{cases} \tag{10}$$

Where $R$ and $r$ are the radio of the tool and the workpiece, which are converted to the effective radius $R_0$. $E_1$, $\mu_1$ and $E_2$, $\mu_2$ are the modulus of elasticity and poisson's ratio of the tool and the workpiece, respectively, which are converted into the effective material parameter $E_0$. $v_1$ and $v_2$ are the linear velocity of the tool and the workpiece at the contact point, and $w$ is the positive pressure on the contact surface of the tool and the workpiece. When the tool comes into contact with calcified tissue and the simulated vascular wall, the film thickness is 0.025 μm and 10.80 μm, respectively. This suggests that smaller film thickness ensures successful material removal when the tool is in contact with the calcified tissue. On the other hand, when the tool is close to the normal vascular wall, the film acts as a protective barrier and prevents damage.

## Finite element simulation model

A 3-D simulation model was created with ABAQUS (version 2016, Fuzhou University), as shown in Fig. 8(a). The tool was meshed with the C3D4 T element type, a four-node coupled thermal tetrahedral element. It is particularly suitable for enhancing the simulation accuracy in the tool's micro-edge region and reducing simulation errors. For improved computational efficiency, the workpiece was meshed using the C3D8RT element type, an eight-node coupled thermal hexahedral element. A 2-D micro-scale cutting simulation model was set up, as shown in Fig. 8(b). The workpiece and tool were meshed using CPE4RT and CPE3 T elements. The workpiece had a 0.4 μm mesh size, with a larger size for its base layer. The model used element deletion to simulate debris generation. The tool was considered an ideal rigid body, neglecting tool wear effects.

The adhesion-sliding friction model[29] was used to handle the debris-tool contact surface. When adhesion occurs, the friction force is equivalent to the maximum shear stress that the material can withstand, denoted as $\bar{\tau}_{max}$. During debris sliding, the shear stress $\bar{\tau}_{max}$ that the material can withstand exceeds the actual shear stress $\bar{\tau}$ in the contact area. As a result, the frictional force is mainly generated by the combination of normal force and friction coefficient. This frictional behavior can be described by the following equation:

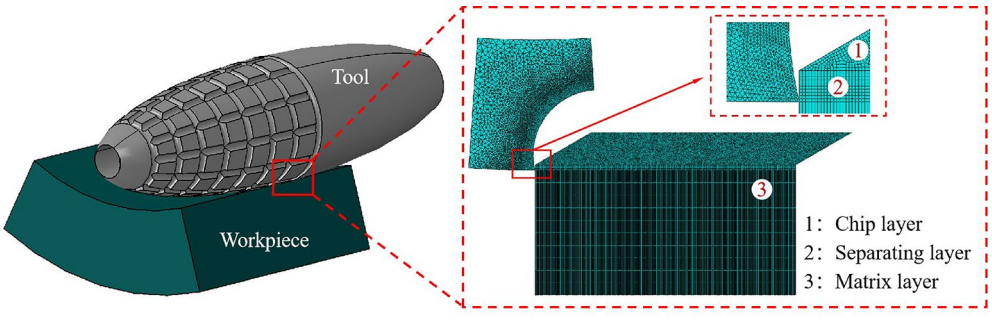


**Fig. 8**. Simulation model. (**a**) 3-D simulation model, (**b**) 2-D simulation model and grid division.

$$\begin{cases} \tau = \mu\,\sigma & \tau < \bar{\tau}_{max} \\ \tau = \bar{\tau}_{max} & \tau \geq \bar{\tau}_{max} \end{cases} \tag{11}$$

The heat generation and conduction in the initial and subsequent deformation zones during material cutting are analyzed by introducing the thermal conduction control equation[30]:

$$\lambda\left(\frac{\partial^2 T}{\partial^2 x}+\frac{\partial^2 T}{\partial^2 y}+\frac{\partial^2 T}{\partial^2 z}\right)+\dot{Q}=\rho\,C_p(u_x\frac{\partial T}{\partial x}+u_y\frac{\partial T}{\partial y}+u_z\frac{\partial T}{\partial z}) \tag{12}$$

where $\lambda$ is the thermal diffusivity, $T$ is the temperature function, $\dot{Q}$ is the heat flux per unit volume, $\rho$ is the material density, $C_p$ is the material specific heat capacity, and $u_x, u_y, u_z$ represent the rates of heat transfer in the $x, y, z$directions, respectively.

The Johnson-Cook (J-C) model was used to analyze the flow stress, offering a comprehensive analysis of how strain, strain rate, and temperature variations influence the plastic behavior of materials[31]:

$$\sigma = [A+B\bar{\epsilon}^{n}][1+C ln\frac{\dot{\bar{\epsilon}}}{\dot{\bar{\epsilon}}_0}][1-((T-T_r)/(T_m-T_r))^m] \tag{13}$$

Where $\sigma$ is the equivalent flow stress, $\bar{\epsilon}$ is the equivalent plastic strain, $\dot{\bar{\epsilon}}$ is the equivalent plastic strain rate, $\dot{\bar{\epsilon}}_0$ reference for the equivalent strain rate; $T$ is the instantaneous temperature, $T_m$ is the melting point of the workpiece material, $T_r$ is the ambient temperature, $A$, $B$, $n$, $C$, and $m$ correspond to the initial yield strength, strain hardening modulus, strain hardening index, strain rate hardening coefficient, and thermal softening coefficient. The J-C constitutive model parameters are shown in Table 3.

The workpiece's initial damage state is evaluated using the J-C damage model and cumulative damage theory[33]. The strain failure condition is determined based on the following equation:

$$D=\sum\frac{\Delta\epsilon_p}{\epsilon_{pf}} \tag{14}$$

Where $\Delta\epsilon_p$ is the growth of the equivalent plastic strain in a single integration step, and $\epsilon_{pf}$ is the equivalent fracture strain under the existing loading conditions. An increase in $D$ to 1 indicates that the material has broken and separated from the workpiece and was subsequently removed. The equivalent fracture strain formula commonly used is as follows:

$$\epsilon_{pf}=(D_1+D_2 exp D_3\sigma^*)(1+D_4 ln\frac{\epsilon_p}{\epsilon_0})(1-D_5((T-T_0)/T_{melt}-T_0)^m \tag{15}$$

The constants $D_1$, $D_2$, $D_3$, $D_4$, and $D_5$, $\epsilon_0$(reference plastic strain), $\epsilon_p$(plastic strain), and the stress ratio $\sigma^*$ collectively define the fracture criterion of the material. To simplify this model, the variable $D_1$ can be set as $\epsilon_{pf}$ while setting the other constants to 0.

## Results and discussion

### Analyse of cutting force

Simulations were carried out with 1.25 mm, 1.5 mm, 1.75 mm, and 2.0 mm tools to explore the effect of process parameters on cutting force. Rotational speeds were set at 60,000 rpm, 80,000 rpm, 100,000 rpm, and 120,000 rpm. Figure 9 shows the results of the simulated cutting forces.

From Fig. 9, it is evident that the cutting forces rise with escalating rotational speed and larger tool diameters. For instance, using the 1.25 mm tool at 60,000 rpm, the force measures 0.29 N. In contrast, for the 2.0 mm tool at the same speed, the cutting force is 0.65 N, roughly 2.27 times greater than the former. At 120,000 rpm, the forces increase to 0.74 N and 1.66 N. The cutting force can be effectively controlled by altering the tool diameter. As rotational speed rises, the increase in force for the smaller diameter tool is comparatively lower, while the force for the larger diameter tool continues to significantly increase, widening the gap between them. This underscores the stability and controllability of using smaller-diameter tools. However, during surgery, higher cutting forces are frequently essential for tissue removal. Therefore, selecting the right tool is crucial for efficiently and accurately removing calcified tissues.

The experiment considered rotational speed, tool size, and workpiece material as variables to analyze the effects of process parameters on forces and explore the underlying mechanisms. The results are shown in Fig. 10,

| | A (Mpa) | B (Mpa) | *n* | C | m |
|---|---|---|---|---|---|
| Bone[32] | 110.6 | 234.8 | 0.4807 | 0.01663 | 1 |
| Human calcified tissue | 150.2 | 278.94 | 0.42 | 0.019 | 1 |

**Table 3**. Parameters of the J-C ontological model.

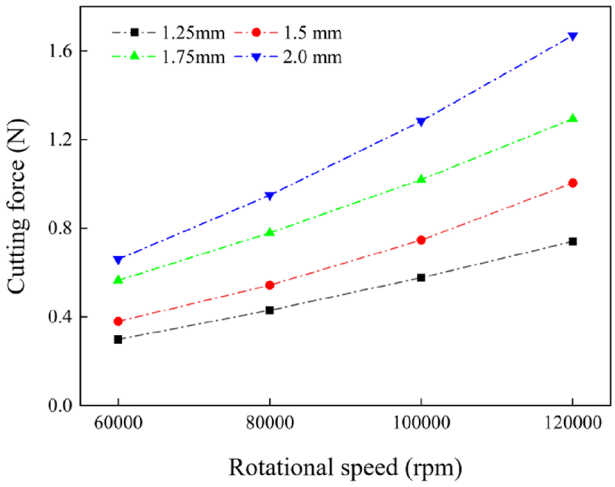


**Fig. 9**. Influence of cutting parameters on force.

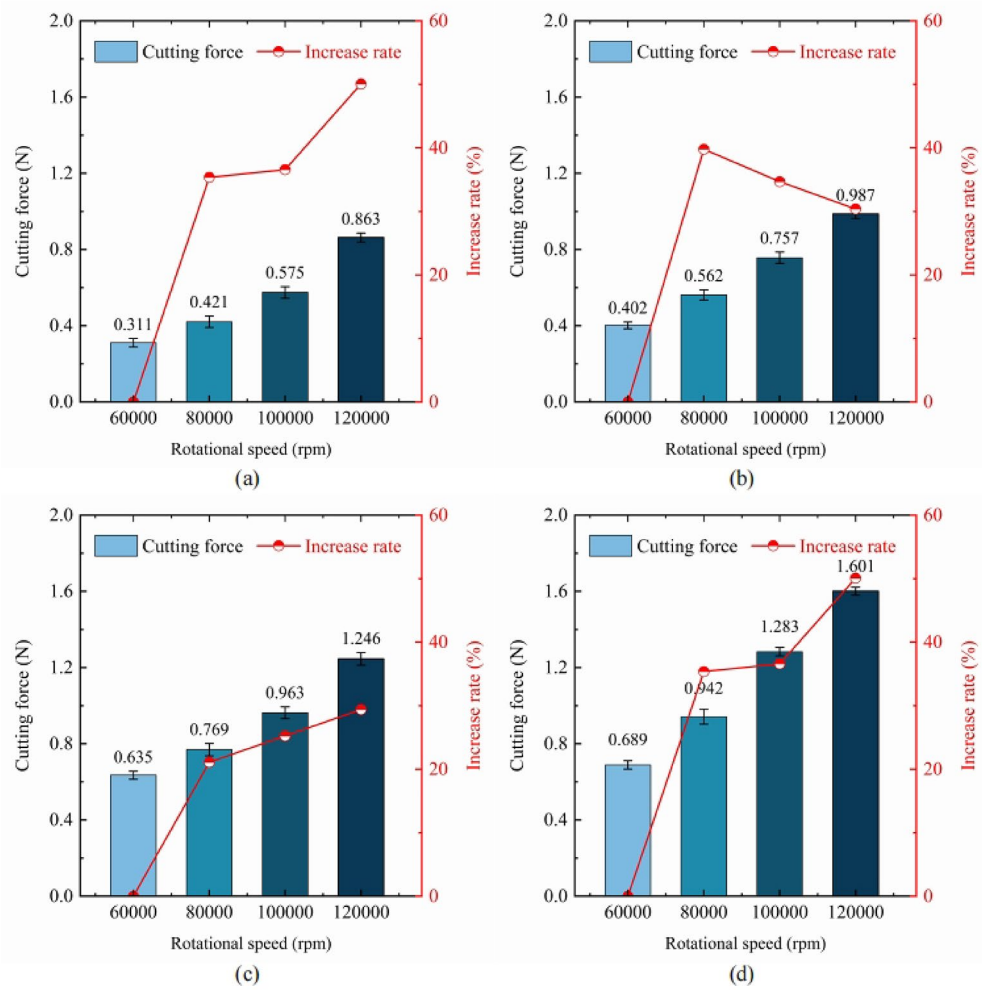


**Fig. 10**. Results of cutting forces at different speeds. (**a**) 1.25 mm, (**b**) 1.50 mm, (**c**) 1.75 mm, and (**d**) 2.00 mm tool.

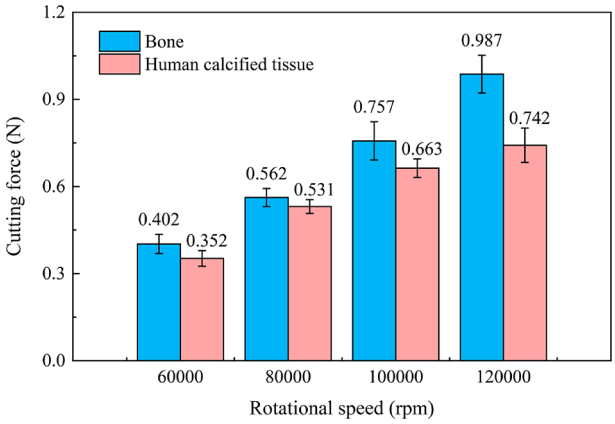


**Fig. 11**. Comparison of cutting forces in different tissues.

| $\omega$ /rpm | $F_B$/N | $F_B{}'$ /N | Relative error/% |
|---|---|---|---|
| 60,000 | 0.362 | 0.402 | 9.95 |
| 80,000 | 0.543 | 0.562 | 3.38 |
| 100,000 | 0.791 | 0.757 | 4.49 |
| 120,000 | 1.062 | 0.987 | 7.60 |

**Table 4**. Comparison of simulation results and experimental of bone.

| $\omega$ /rpm | $F_B$/N | $F_B{}'$ /N | Relative error/% |
|---|---|---|---|
| 60,000 | 0.343 | 0.352 | 2.56 |
| 80,000 | 0.494 | 0.531 | 6.97 |
| 100,000 | 0.648 | 0.663 | 2.26 |
| 120,000 | 0.795 | 0.742 | 7.14 |

**Table 5**. Comparison of simulation results and experimental of calcified tissue force.

revealing a notable rise in forces with increasing rotational speed. When the speed increased from 60,000 rpm to 120,000 rpm, the force for the 1.25 mm tool surged from 0.311 N to 0.863 N, for the 1.5 mm tool from 0.402 N to 0.987 N, for the 1.75 mm tool from 0.635 N to 1.246 N, and for the 2.0 mm tool from 0.689 N to 1.601 N. The increase rates are 177.49%, 145.52%, 96.22%, and 132.37%.

In this study, a comparative experiment was performed using human calcified tissue. Due to the limited number of tissue samples, a complete orthogonal experiment could not be performed, and testing was solely carried out using a 1.5 mm tool. The force results are shown in Fig. 11.

From Fig. 11, it is evident that the force increases with the increase in rotational speed. At 120,000 rpm with a 1.5 mm diameter tool, the forces for bone and calcified tissue were 0.987 N and 0.742 N, which are notably below the medical regulation threshold of 5 N[5], suggesting that the novel tool offers enhanced safety and reliability for cutting procedures. Simultaneously, the rise in speed accentuates the variance in forces among distinct tissues. This trend can be ascribed to a multitude of contributing factors. Firstly, higher speed leads to increased the tool's kinetic energy, resulting in more intense collisions between the tool and tissue. Secondly, bone has slightly higher hardness and elastic modulus in contrast to calcified tissue. Therefore, under the same force, bone can more effectively resist the force. A comparison between the measured forces and the theoretical values from the force model is detailed in Tables 4 and 5. Where $\omega$ is the rotational speed, $F_B$ is the force simulation results, and $F_B{}'$ is the experimental results. The relative error of the bone cutting force model is less than 10% at 80,000 rpm and 100,000 rpm. For the calcified tissue, the relative error of the force model is 2.56% and 2.26% at 60,000 rpm and 100,000 rpm, respectively. These findings indicate the efficacy of the force model in accurately predicting experimental outcomes.

## Analyse of cutting temperature

A complete cutting cycle from the tool's initial contact with the material to complete detachment. The tool tip temperature change is shown in Fig. 12. Initially, the tool tip temperature rises with cutting time but rapidly decreases and stabilizes at ambient temperature as the tool disengages. The temperature range $\Delta T$ was recorded as the experimental result.

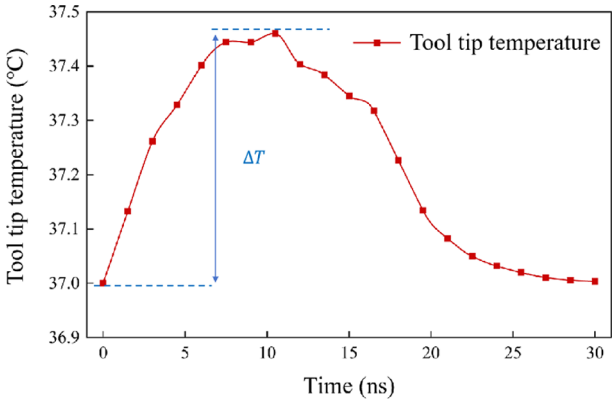


**Fig. 12**. Tool tip temperature.

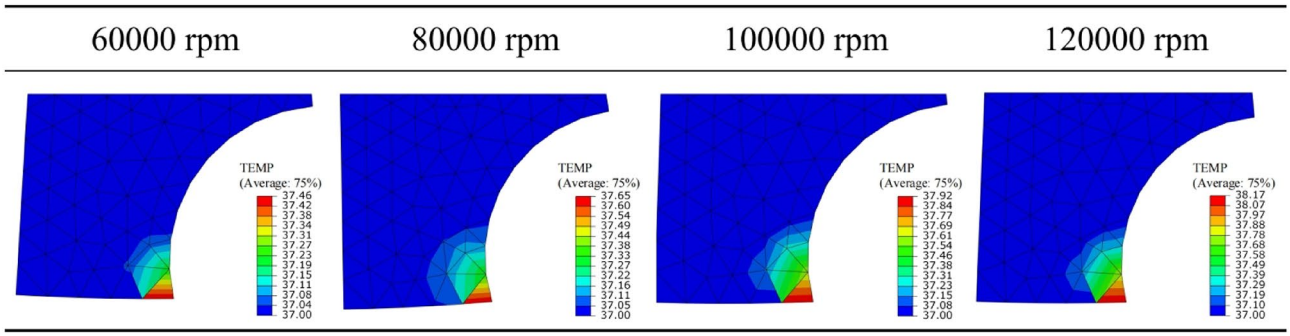


**Fig. 13**. Effect of rotational speed on temperature rise of bone.

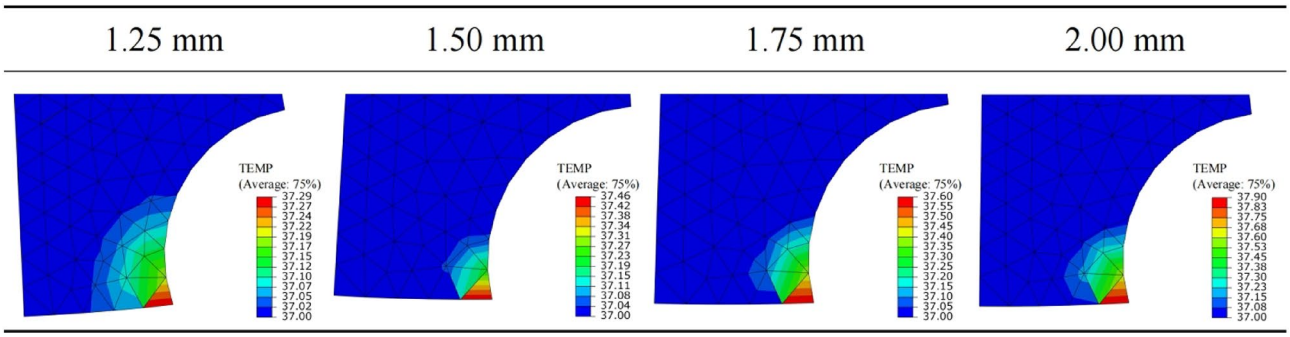


**Fig. 14**. Effect of cutting tool size on temperature rise of bone.

Figure 13 demonstrates that the most substantial temperature increase occurs at the tool tip's contact region with debris. As speed increases, the surface temperature rises from 0.46 ℃ to 1.17 ℃, resulting in a temperature increment of 154.35%. Figure 14 shows the influence of tool size on temperature. Simulation results show that increasing the tool size will significantly increase the cutting temperature, rising from 0.29 ℃ to 0.90 ℃, achieving a remarkable rise of 310.34%. Larger tools may generate higher heat in the cutting contact area, which could be attributed to the increased contact area and the enhanced frictional forces. At the same speed, the impact effect of the large tool is stronger in the collision, and the depth of the tool invasion into the material increases, resulting in a larger actual contact area and aggravating the heat exchange. Figure 15 shows the temperature rise differences among different tissues. When machining calcified tissue, the surface temperature increases from 0.36 ℃ to 1.04 ℃, resulting in a change of 288.88%. Furthermore, it was observed that although there are differences in cutting temperatures between the two tissues, the trends and numerical values are relatively close, indicating the feasibility of using bone for mechanistic studies.

Temperature experiments were conducted with the simulated blood preheated and stabilized at 37 ℃, with a flow rate of 32 ml/min. The average temperature rise are shown in Fig. 16.

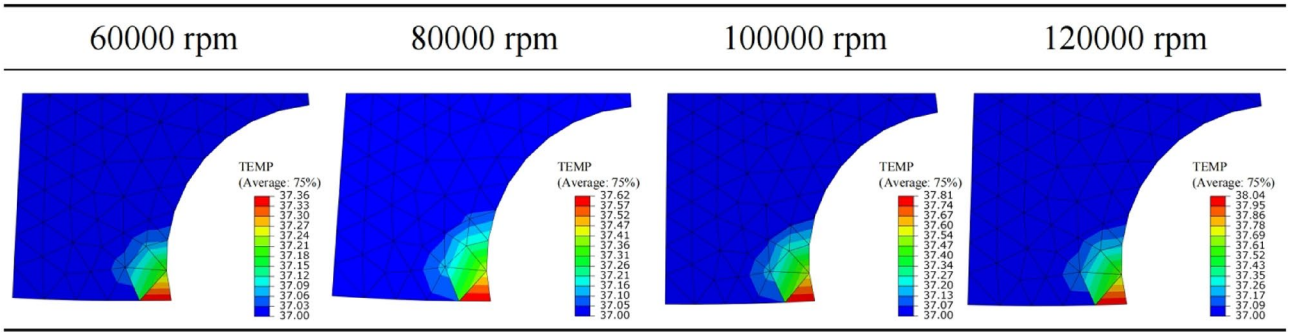


**Fig. 15**. Effect of rotational speed on temperature rise of human calcified tissue.

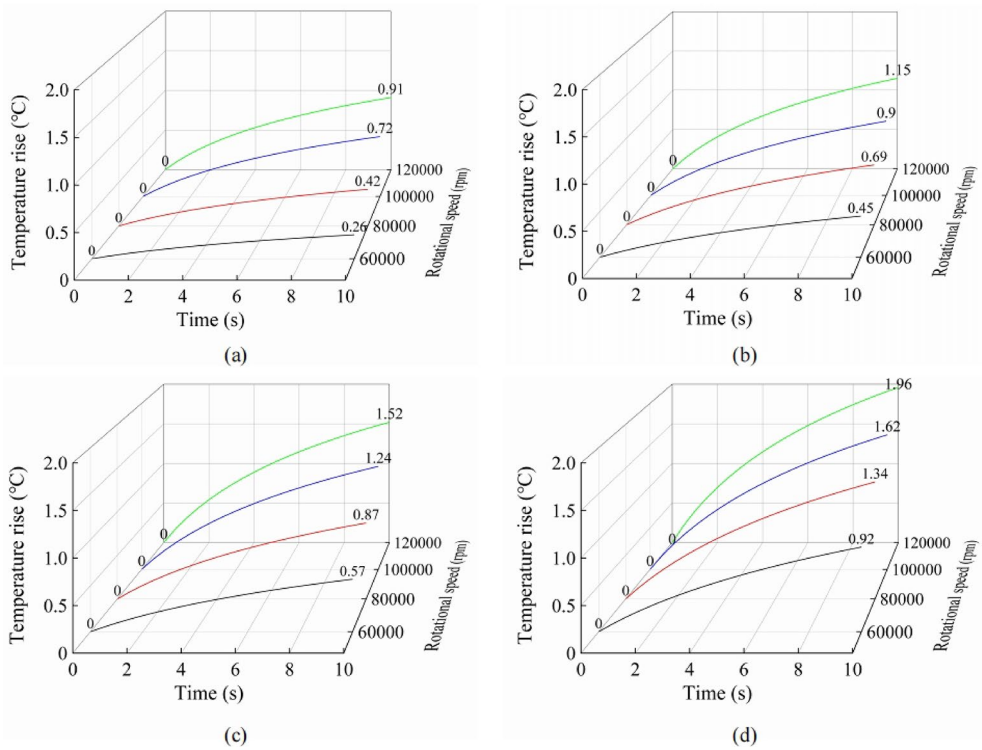


**Fig. 16**. Results of temperature rise under different parameters. (**a**) 1.25 mm, (**b**) 1.50 mm, (**c**) 1.75 mm, and (**d**) 2.00 mm tool.

From Fig. 16, it can be observed that as the speed increases from 60,000 rpm to 120,000 rpm, a notable temperature increase is evident. The temperature rise of the four tools increased from 0.26 ℃, 0.45 ℃, 0.57 ℃, and 0.92 ℃ to 0.91 ℃, 1.15 ℃, 1.52 ℃, and 1.96 ℃, the increase rate are 250.0%, 155.5%, 166.7%, and 113.1%. The increased speed leads to a rapid growth in frictional force between the tool's micro-edge and calcified tissue, resulting in the accumulation of frictional heat. This phenomenon increases the conversion rate of mechanical energy into thermal energy, leading to a rise in system temperature. Moreover, at high speed, cutting tools lose energy due to collisions with tissue and force generation, converting this loss into heat and raising temperatures in the system. At the same time, the blood cooling effect at high speeds may deteriorate due to the microcavitation effect, resulting in the inability to fully dissipate the heat generated by friction, further aggravating the temperature rise. On the other hand, larger tools exert higher dynamic loads during cutting, converting mechanical energy into heat efficiently, leading to a rapid temperature rise in the cutting region, especially under high-speed or heavy-load conditions. As a result, the temperature in the cutting region rises rapidly and significantly.

Check experiments were performed using human calcified tissue, and the results are shown in Fig. 17. It is evident that the trend of temperature rise increasing with higher speed remains consistent. At 120,000 rpm, the temperature rise is measured to be 1.152 ℃ and 1.023 ℃, below the maximum 6 ℃ rise in human tissues. This indicates that the tool-induced temperature increase remains within a safe range[5]. As the speed increases from

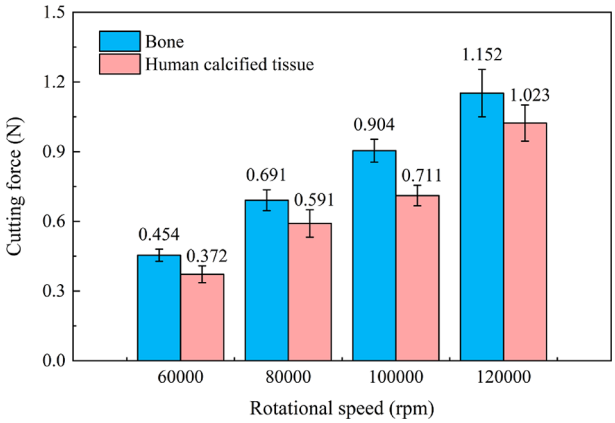


**Fig. 17**. Comparison of the temperature rise of different tissues (1.50 mm tool).

| $\omega$ (rpm) | $T_B$ (℃) | $T_B'$ (℃) | Relative error (%) |
|---|---|---|---|
| 60,000 | 0.46 | 0.45 | 2.22 |
| 80,000 | 0.65 | 0.69 | 5.80 |
| 100,000 | 0.92 | 0.90 | 2.22 |
| 120,000 | 1.17 | 1.15 | 1.74 |

**Table 6**. Comparison of bone cutting temperature rise modeling and experimental results.

| $\omega$ (rpm) | $T_C$ (℃) | $T_C'$ (℃) | Relative Error (%) |
|---|---|---|---|
| 60,000 | 0.36 | 0.37 | 2.70 |
| 80,000 | 0.62 | 0.59 | 5.08 |
| 100,000 | 0.81 | 0.71 | 14.08 |
| 120,000 | 1.04 | 1.02 | 1.96 |

**Table 7**. Comparison of calcified tissue cutting temperature rise model and experimental results.

60,000 rpm to 120,000 rpm, the temperature difference between the two tissues expands from a minimum of 0.08 ℃ to 0.19 ℃. The temperature rise difference remains within 0.2 ℃, reaffirming the feasibility of using bone as a substitute for calcified tissue.

The comparison of experimental and simulation temperature rise results are shown in Tables 6 and 7. $T_B$ is the temperature simulation result, $T_B'$ is the experimental result. When the speed increases from 60,000 rpm to 120,000 rpm, the modeling error for bone's cutting temperature rise consistently stays below 6%. However, at 100,000 rpm, the error for calcified tissue is 14.08%. This discrepancy can be attributed to the fixed material properties set in the simulation model, which assumes a linear relationship for temperature rise variation and deviates slightly from the experimental results. Nonetheless, at other speeds, the relative error remains under control at 6% or lower, demonstrating the model's effectiveness in predicting experimental outcomes.

## Analyse of debris size

Excessive debris size is a major cause of complications such as distal capillary blockage and slow blood flow. Hence, this study focuses on investigating how RA process parameters impact debris size. Simulation analysis was conducted using consistent settings from Sect. 3.2, with results shown in Figs. 18 and 19,20.

In Fig. 18, the debris displays a block-like, non-continuous morphology. As the speed increases, there is a notable decrease in the average debris size from 14.0 μm to 8.0 μm. This is due to the increased effect of the larger cutting force at high speed on the material surface. It leads to a denser distribution of microcracks, resulting in finer and more uniform material fragmentation. Figure 19 shows the impact of different tool sizes on debris size. As the tool size increases, the debris size also increases proportionally. The average size increases from 11.5 μm to 16.6 μm. Figure 20 shows the debris size produced during the cutting of calcified tissue. As the speed increases, the debris size decreases from 12.8 μm to 7.2 μm, representing a reduction of 43.75%.

Debris size was measured under different parameters, with five independent experiments conducted for each parameter set. Results are shown in Fig. 21. Notably, at 120,000 rpm, the debris sizes were measured as 7.80 μm, 8.71 μm, 10.07 μm, and 12.69 μm, respectively. The trend shows an increase in size with larger tool diameters, likely due to increased heat accumulation affecting material deformation and promoting larger debris formation.

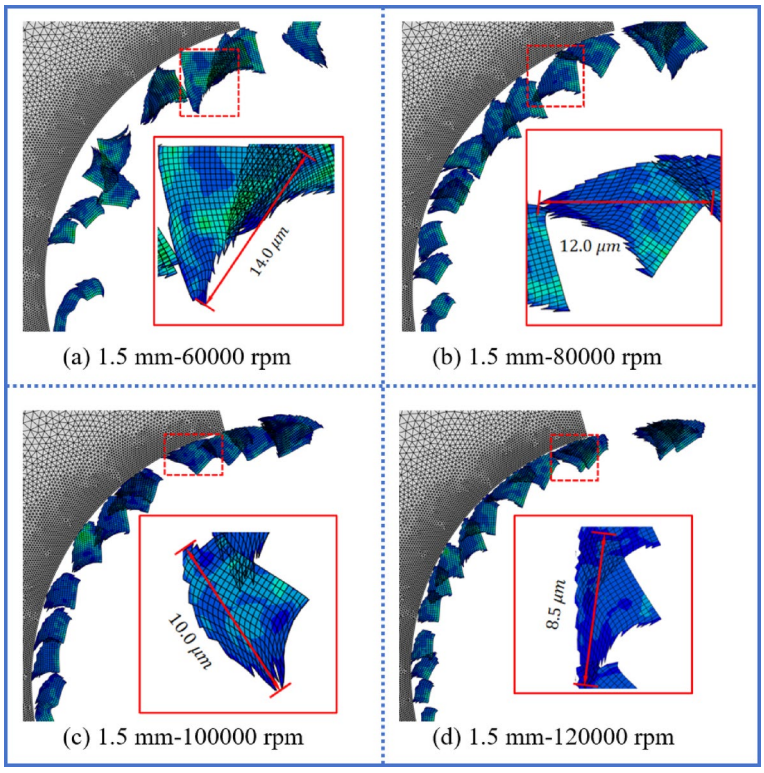


**Fig. 18**. Effect of rotational speed on the debris size.

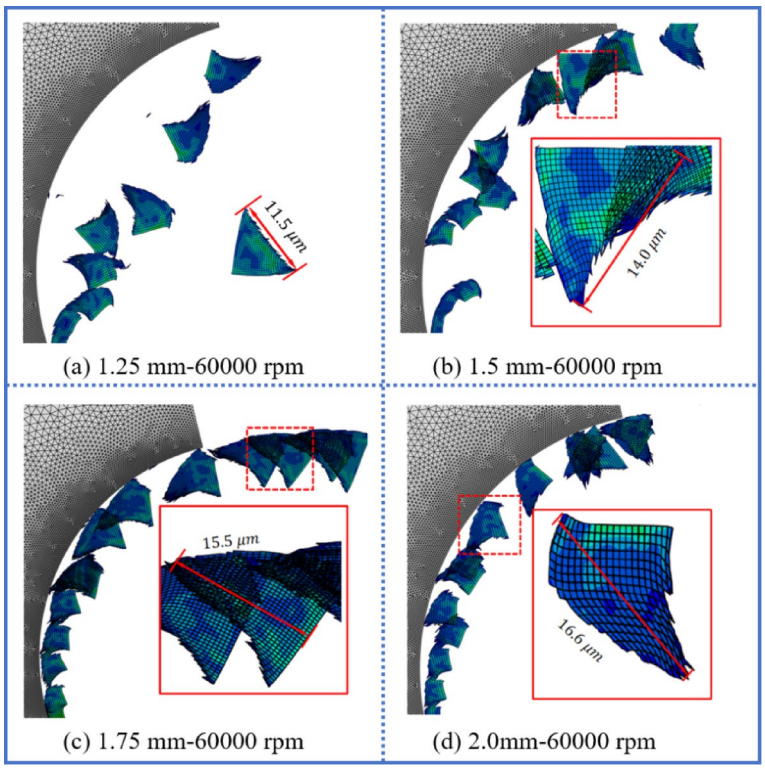


**Fig. 19**. Effect of tool size on the debris size.

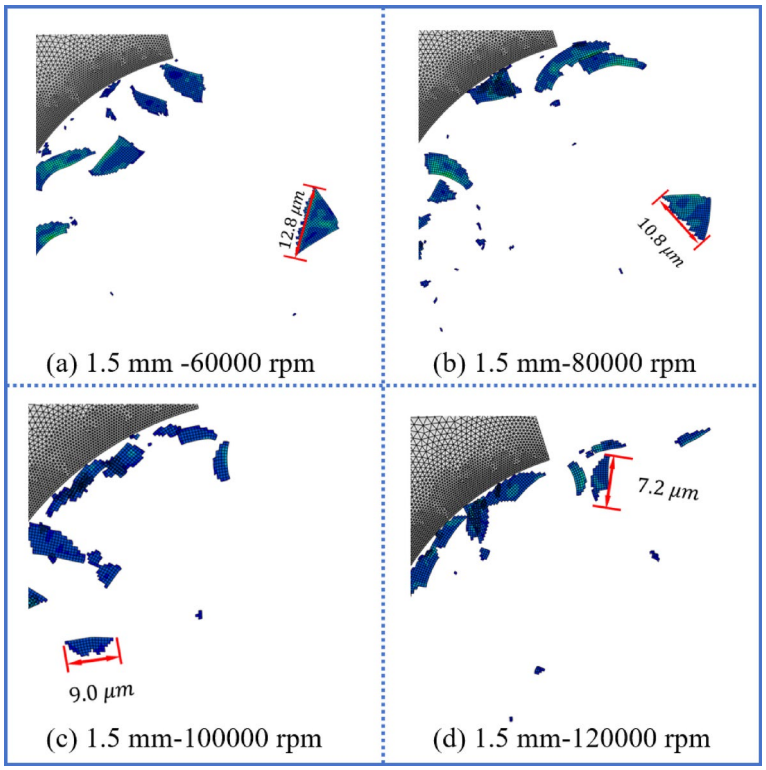


**Fig. 20**. Effect of rotational speed on the particle size of debris from calcified tissue.

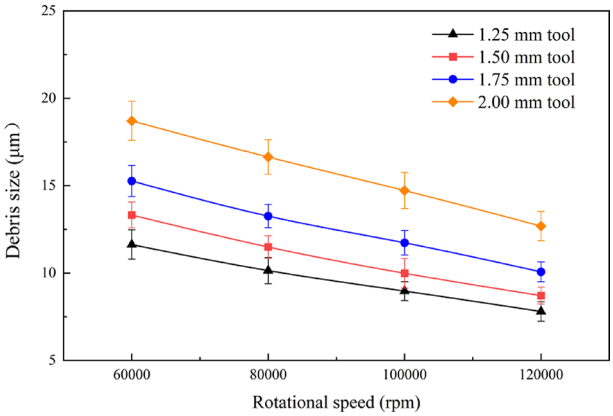


**Fig. 21**. Results of debris size under different parameters.

Conversely, as speed rises, the debris size gradually decreases, revealing a significant inverse correlation between debris size and cutting speed. When the speed is increased from 60,000 rpm to 120,000 rpm, the debris sizes decrease from 11.63 μm, 13.20 μm, 15.27 μm, and 18.71 μm to 7.80 μm, 8.68 μm, 10.07 μm, and 12.69 μm, respectively. This trend is influenced by multiple factors. Firstly, increasing the speed accelerates the tool's orbit motion speed, thereby reducing the duration of tool action at each contact point, leading to less material removal per contact. Secondly, the higher speed boosts the shear strain rate during cutting, potentially enhancing material fracture and deformation, thereby contributing to debris refinement.

To provide a more visual representation of the debris morphology characteristics under different parameters, the debris images are grouped and displayed in Fig. 22.

Additionally, this study also analyzed the surface morphology of the specimens after RA. The measurement model was sectioned along the centerline and the inner surface was cleaned. The surface wear was measured using a 3D profilometer, and the cutting depth was extracted as shown in Fig. 23.

From Fig. 23, it can be observed that at 60,000 rpm, the cutting depths for the four tools are 9.542 μm, 12.045 μm, 13.876 μm, and 16.425 μm, respectively. Depth increases with tool diameter, as larger tools carry more energy, resulting in higher radial pressure on calcified tissue. Check experiments on calcified tissue were

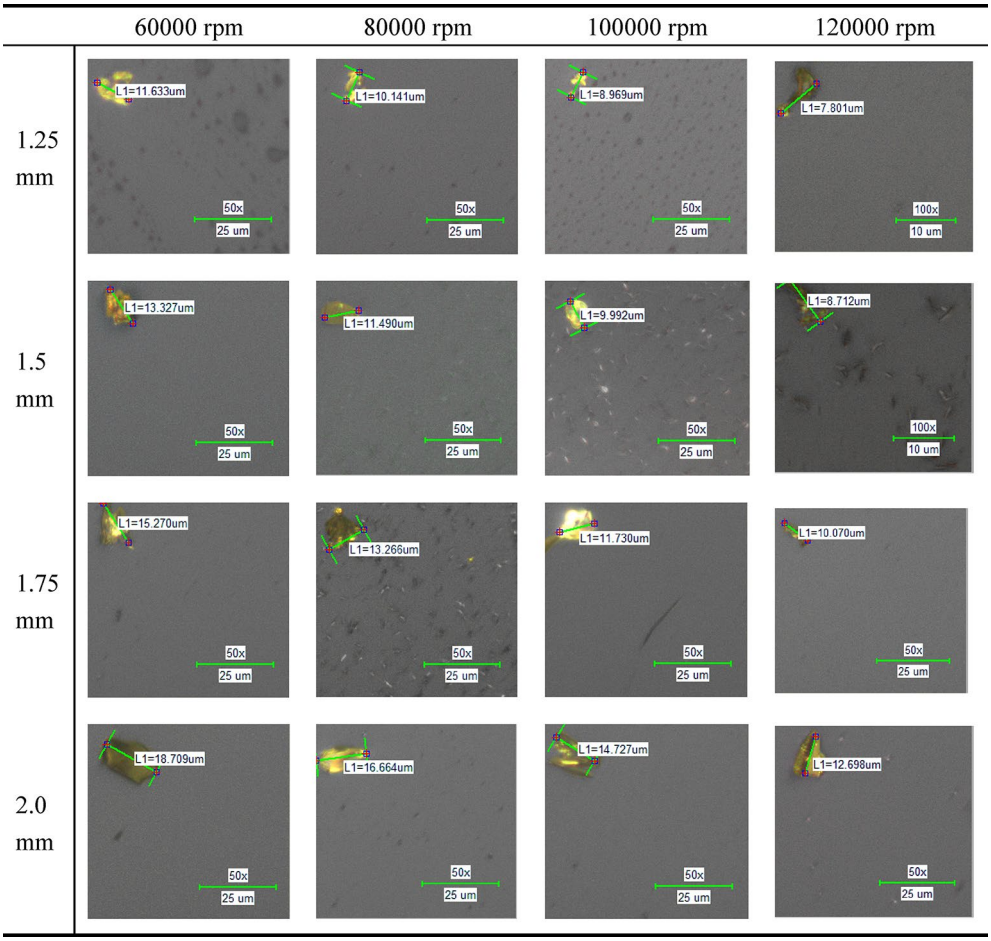


**Fig. 22**. Effect of different parameters on debris morphology.

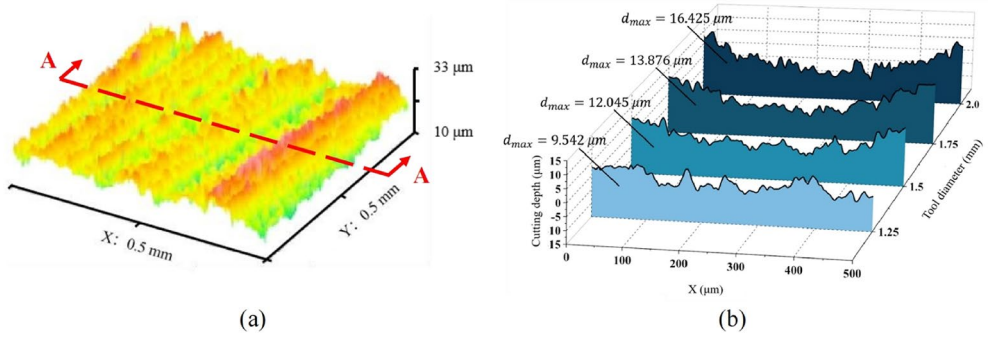


**Fig. 23**. Effect of different tool sizes on surface morphology. (**a**) The wear morphology of the specimen surface, and (**b**) the cutting depth under different parameters.

conducted, and the results are shown in Fig. 24. The data indicates a reduction in debris size with escalating rotational speed. The average debris size of the two tissues measured under different parameters were close to each other.

The comparison between experimental and simulated results are shown in Tables 8 and 9. $D_B$ is the simulation results, $D_B{}'$ is the experimental results. As the speed increases from 60,000 rpm to 100,000 rpm, the simulation results for bone and calcified tissue show an error of less than 10%. However, at 120,000 rpm, the relative error is 15.49%. This discrepancy may be attributed to factors such as the mismatch between the tool design, processing parameters, or lubrication conditions. These factors can lead to issues such as vibration and heat accumulation, which can influence the debris morphology. In general, the debris model demonstrates good predictive capability for the experimental results.

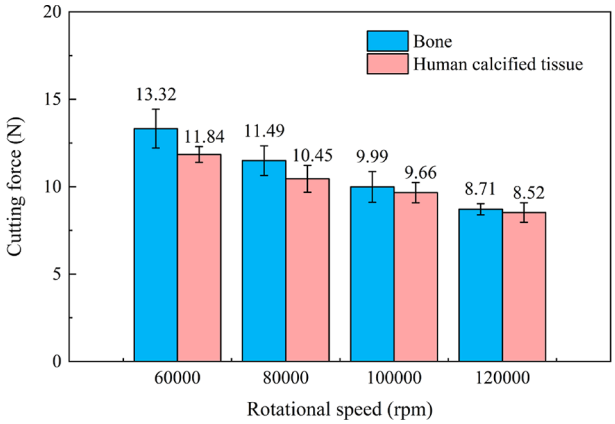


**Fig. 24**. Comparison of debris size for different tissues.

| $\omega$ (rpm) | $D_B$ (μm) | $D_B'$ (μm) | Relative error (%) |
|---|---|---|---|
| 60,000 | 14 | 13.32 | 5.11 |
| 80,000 | 12 | 11.49 | 4.44 |
| 100,000 | 10 | 9.99 | 0.10 |
| 120,000 | 8.5 | 8.71 | 2.41 |

**Table 8**. Comparison of simulated debris size with experimental results.

| $\omega$ (rpm) | $D_C$ (μm) | $D_C'$ (μm) | Relative error (%) |
|---|---|---|---|
| 60,000 | 12.8 | 11.84 | 8.11 |
| 80,000 | 10.8 | 10.45 | 3.35 |
| 100,000 | 9 | 9.66 | 6.83 |
| 120,000 | 7.2 | 8.52 | 15.49 |

**Table 9**. Comparison of simulated calcified tissue debris size with experimental results.

## Conclusion

This study focuses on the mechanism of removing coronary artery calcification tissues through RA. The tool kinematics and dynamics were analyzed, and the force, temperature, debris and surface wear morphology in the process of material removal were analyzed to clarify the influence of process parameters on the results. An RA simulation model was developed and its accuracy was verified using experimental data. The main findings of this research are as follows:

(1) The tool rotates around its axis while simultaneously performing a orbit motion along blood vessel. Based on the theory of single-disc steady-state vortex rotor, it is known that the orbit motion frequency is positively correlated with the rotation frequency. The tool motion pattern can be described as "collision-bounce-collision," where intermittent contact of the tool with the calcified tissue facilitates its removal. The calculated fluid dynamic pressure film on the calcification and the blood vessel is found to be 0.025 μm and 10.8 μm, respectively. This indicates that calcified tissue can be effectively removed without damaging the blood vessel.

(2) A 3-D RA simulation model and a 2-D microstructural equivalent simulation model were established to reveal the removal mechanism from macroscopic forces and heat to microscopic debris formation. The accuracy of the simulation models was validated through experimental verification.

(3) This study analyzed the forces and temperature rise under different cutting parameters, revealing the patterns of force and temperature variation with process parameters. Increasing the tool size and rotational speed leads to an increase in cutting force and temperature. For the 2.00 mm tool at 120,000 rpm, the maximum simulated and experimental forces were 1.062 N and 0.987 N, respectively. The maximum temperature rise was measured as 1.17℃ and 1.15℃. The simulated results exhibit a relative error within 10% compared to the experimental data.

(4) The novel tool effectively controls the debris size. Simulation results show that using 1.5 mm tool at four different speeds, the debris size for cutting bone ranges from 14 μm to 8.5 μm, while for calcified tissue, it ranges from 12.8 μm to 7.2 μm. These sizes are significantly below the clinical safety threshold for debris. Experiments revealed that increasing rotational speed reduces debris size, whereas larger tool sizes increase debris size.

This study introduces a novel cutting tool, demonstrating its outstanding performance in suppressing force, temperature, and chip size, offering a new perspective for optimizing the therapeutic effects of RA. Simultaneously, a detailed investigation into the RA mechanism facilitates physicians in making more rational selections of parameters to reduce the occurrence of complications. However, it still possesses some limitations, such as the lack of consideration of the effects of liquids in the simulation and the disparities between the experimental environment and the actual human body environment. Therefore, future work involve conducting human experiment, alongside contemplating the integration of advanced processing methods from engineering practices, such as vibration assistance, to enhance the therapeutic effects of RA, so as to make it further popularized.

## Data availability

All data generated or analysed during this study are included in this published article.

Received: 19 September 2024; Accepted: 5 May 2025
Published online: 08 May 2025

## References

1. Hou, P. B. et al. Macrophage polarization and metabolism in atherosclerosis. *Cell. Death Dis.* **14**, 691 (2023).
2. Björkegren, J. L. M. & Lusis, A. J. Atherosclerosis: recent developments. *Cell* **185**, 1630–1645 (2022).
3. Libby, P., Ridker, P. M. & Maseri, A. Inflammation and atherosclerosis. *Circulation* **105**, 1135–1143 (2002).
4. Bhatt, D. L. Percutaneous coronary intervention in 2018. *JAMA* **319**, 2127–2128 (2022).
5. Sharma, S. K. et al. North American expert review of rotational atherectomy. *Circ. Cardiovasc. Interv.* **12**, e007448 (2019).
6. Pagnotta, P. et al. Rotational atherectomy in resistant chronic total occlusions. *Catheter Cardiovasc. Interv.* **76**, 366–371 (2010).
7. Gupta, T. et al. Rotational atherectomy: a contemporary appraisal. *Interv Cardiol.* **14**, 182 (2019).
8. Taneva, G. T. et al. Midterm outcomes of rotational atherectomy-assisted endovascular treatment of severe peripheral arterial disease. *J. Vasc Surg.* **79**, 887–892 (2024).
9. Huang, W. C. et al. Short-term and long-term clinical outcomes of rotational atherectomy in resistant chronic total occlusion. *J. Interv Cardiol.* **31**, 458–464 (2018).
10. Elbasha, K. et al. Long-Term Outcomes after Rotational Atherectomy for Calcified Chronic Total Occlusion versus Nonchronic Total Occlusion Coronary Lesions. *J Interv Cardiol.* 2593189 (2022). (2022).
11. Rheude, T. et al. Rotational atherectomy or balloon-based techniques to prepare severely calcified coronary lesions. *JACC-Cardiovasc Inte.* **15**, 1864–1874 (2022).
12. Allali, A. et al. Rotational atherectomy of calcified coronary lesions: current practice and insights from two randomized trials. *Clin. Res. Cardiol.* **112**, 1143–1163 (2023).
13. Yoshizaki, T. et al. Impact of atherothrombotic risk stratification in patients with heavily calcified lesions following rotational atherectomy. *J. Cardiol.* **83**, 37–43 (2024).
14. Édes, I. F. et al. Clinical predictors of mortality following rotational catherectomy and stent implantation in high-risk patients: A single center experience. *Catheter Cardiovasc. Interv.* **86**, 634–641 (2015).
15. Taniguchi, Y. et al. Rotational atherectomy to left circumflex ostial lesions: tips and tricks. *Cardiovasc. Interv Ther.* **38**, 367–374 (2023).
16. Wu, J. et al. The incidence of complication in the perioperative period of rotational atherectomy in patients with acute coronary syndrome: A retrospective study of low speed versus high speed. *Am. J. Cardiol.* **207**, 121–129 (2023).
17. Sakakura, K. et al. Study design and rationale for comparison of the incidence of slow flow following rotational atherectomy to severely calcified coronary artery lesions between short single session and long single session: the randomized ROTASOLO trial. *Cardiol. J.* **30**, 483–488 (2023).
18. Zheng, Y. et al. Computational fluid dynamics modeling of the burr orbital motion in rotational atherectomy with particle image velocimetry validation. *Ann. Biomed. Eng.* **46**, 567–578 (2018).
19. Gao, C. et al. Performance of novel 3D printing tools in removing coronary-artery calcification tissue. *Biodes Manuf.* **6**, 390–404 (2023).
20. Liu, Y. et al. Catheter thermal energy generation and temperature in rotational atherectomy. *Med. Eng. Phys.* **70**, 29–38 (2019).
21. Shammas, N. W. et al. Pr eventing L O Wer ex t remity distal E mbolization using emboli C fil t Er protection: results of the PROTECT registry. *J. Endovasc Ther.* **15**, 270–276 (2008).
22. Abdurrazzak, A. & Gehani, M. R. R. Can rotational atherectomy cause thermal Tissure damage a study of the potential heating and thermal Tissure effects of a rotattional atherectomy device. *Cardiovasc. Intervent Radiol.* **21**, 481–486 (1998).
23. Nakao, M., Tsuchiya, K., Maeda, W. & Iijima, D. A rotating cutting tool to remove hard cemented deposits in heart blood vessels without damaging soft vessel walls. *CIRP Ann. Manuf. Technol.* **54**, 37–40 (2005).
24. Zheng, Y. et al. Multigrain smoothed particle hydrodynamics and Hertzian contact modeling of the grinding force in atherectomy. *J. Manuf. Sci. Eng.* **141**, 041015 (2019).
25. Kim, M. H. et al. A rotational ablation tool for calcified atherosclerotic plaque removal. *Biomed. Microdevices*. **13**, 963–971 (2011).
26. Zhu, Z. et al. Numerical analysis of stress force on vessel walls in atherosclerotic plaque removal through coronary rotational atherectomy. *Micromachines* **14**, 2148 (2023).
27. Crandall, S. H. & Rotordynamics *Nonlinear Dynamics and Stochastic Mechanics* first edn (CRC, 2018).
28. Hamrock, B. J., Schmid, S. R. & Jacobson, B. O. *Fundamentals of Fluid Film Lubrication* (NASA, 2004).
29. Zorev, N. N. Inter-relationship between shear processes occurring along tool face and shear plane in metal cutting. *Int. Res. Prod. Eng.* **49**, 143–152 (1963).
30. Zhang, Q. et al. The piston machining residual stress finite element calculation and experiment research. *Chin. Intern. Combust. Engine Eng.* **35**, 100–106 (2014).
31. Johnson, G. R. A constitutive model and data for metals subjected to large strains, high strain rates and high temperatures. Proceedings of the 7th International Symposium on Ballistics, The Hague, Netherlands, (1983).
32. Alam, K., Khan, M. & Silberschmidt, V. V. 3D finite-element modelling of drilling cortical bone: temperature analysis. *J. Med. Biol. Eng.* **34**, 618–623 (2014).
33. Hillerborg, A., Modéer, M. & Petersson, P. E. Analysis of crack formation and crack growth in concrete by means of fracture mechanics and finite elements. *Cem. Concr Res.* **6**, 773–781 (1976).

## Acknowledgements

We appreciate Fujian Medical University Union Hospital for providing human calcified tissue and relevant medical guidance for this study.

## Author contributions

All authors contributed to the study conception and design. Material preparation, data collection and analysis were performed by Chuhang Gao, Wu Fang and Ziyu Cui, The first draft of the manuscript was written by Chuhang Gao, Zhaoju Zhu and Jialiang Zhu; draft review performed by Mingcheng Fang and Bingwei He. All authors read and approved the final manuscript.

## Funding

This work was funded by the National Natural Science Foundation of China, Grant numbers [52205455], Fujian Provincial Health Technology Project, Grant numbers [2023QNA004] and National Market Supervision Administration Technology Project of China, Grant numbers [2021101560].

## Declarations

## Competing interests

The authors declare no competing interests.

## Additional information

**Correspondence** and requests for materials should be addressed to M.F. or Z.Z.